



## Full length article

## Fast synchrotron X-ray tomographic quantification of dendrite evolution during the solidification of Mg–Sn alloys



Sansan Shuai<sup>a, b, c</sup>, Enyu Guo<sup>b, d, \*\*\*</sup>, A.B. Phillion<sup>d, e</sup>, Mark D. Callaghan<sup>b, d</sup>, Tao Jing<sup>a, \*\*</sup>, Peter D. Lee<sup>b, d, \*</sup>

<sup>a</sup> Key Laboratory for Advanced Materials Processing Technology, Ministry of Education, School of Materials Science and Engineering, Tsinghua University, Beijing, 100084, China

<sup>b</sup> School of Materials, The University of Manchester, Oxford Road, Manchester, M13 9PL, UK

<sup>c</sup> Department of Materials Engineering, Shanghai University, Shanghai, 200072, China

<sup>d</sup> Research Complex at Harwell, RAL, Didcot, OX11 0FA, UK

<sup>e</sup> Department of Materials Science and Engineering, McMaster University, Hamilton, L8S 4L7, Canada

## ARTICLE INFO

## Article history:

Received 2 June 2016

Received in revised form

15 July 2016

Accepted 23 July 2016

Available online 4 August 2016

## Keywords:

Magnesium alloy

Dendritic growth

3-D X-ray tomography

Coarsening mechanism

Crystallographic orientation

## ABSTRACT

The evolution of dendritic microstructures during the solidification of a Mg–15 wt%Sn alloy was investigated *in situ* via fast synchrotron X-ray microtomography. To enable these *in situ* observations a novel encapsulation method was developed and integrated into a fast, pink beam, imaging beamline at Diamond Light Source. The dendritic growth was quantified with time using: solid volume fraction, tip velocity, interface specific surface area, and surface curvature. The influence of cooling rate upon these quantities and primary phase nucleation was investigated. The primary dendrites grew with an 18-branch, 6-fold symmetry structure, accompanied by coarsening. The coarsening process was assessed by the specific surface area and was compared with the existing models. These results provide the first quantification of dendritic growth during the solidification of Mg alloys, confirming existing analytic models and providing experimental data to inform and validate more complex numeric models.

© 2016 Acta Materialia Inc. Published by Elsevier Ltd. This is an open access article under the CC BY license (<http://creativecommons.org/licenses/by/4.0/>).

## 1. Introduction

Magnesium (Mg) based alloys, with their high specific strength to weight ratio, are attractive structural materials for a wide range of applications due to society's demand for light weighting in the transportation industries [1]. A large number of Mg components are fabricated through shape casting processes, owing to Mg's excellent castability, allowing for the creation of highly intricate shapes. The microstructure formed during casting is diverse, consisting of dendrites, eutectics, and multi-component precipitate phases. Dendrites, the most common primary phase structure in commercial Mg alloys, result from progressive instabilities in the

solid/liquid interface during solidification [2–4]. Since shape castings experience only a minimal amount of downstream processing, this as-cast dendritic structure plays an important role in controlling the final mechanical properties.

The morphology of dendrites is strongly dependent on the applied cooling rate during solidification. At higher cooling rates, the diffusion of heat can control the growth morphology in alloys, often forming a well-defined dendritic structure with primary- and secondary order branches. However, the dendritic morphology at low cooling rates is determined by solute diffusion, and Mg alloys can form a degenerate microstructure in this regime [2,5–7]. The formation and evolution of many dendritic structures is not fully understood. Metallography performed on specimens quenched at different temperatures to interrupt the solidification is the most frequent method of analysis. Metallography provides a 2D image of the solidification microstructure (and more recently 3D via serial sectioning) [8,9]; however, structure evolution can only be statistically compared as the technique is destructive, and it is difficult to separate the primary and quenched structures (especially in HCP crystals such as Mg). *Ex situ* 3D microstructures can also be obtained using X-ray microtomography on quenched specimens

\* Corresponding author. School of Materials, The University of Manchester, Oxford Road, Manchester, M13 9PL, UK.

\*\* Corresponding author. School of Materials Science and Engineering, Tsinghua University, Beijing, 100084, China.

\*\*\* Corresponding author. School of Materials, The University of Manchester, Oxford Road, Manchester, M13 9PL, UK.

E-mail addresses: [enyu.guo@manchester.ac.uk](mailto:enyu.guo@manchester.ac.uk) (E. Guo), [jingtao@mail.thu.edu.cn](mailto:jingtao@mail.thu.edu.cn) (T. Jing), [peter.lee@manchester.ac.uk](mailto:peter.lee@manchester.ac.uk) (P.D. Lee).

[10–13], however the same challenges arise.

*In situ* observation allows for direct visualization of solidification microstructure as it develops in real-time. This approach was initially conducted in 2D on organic analogues to metals [14–17], and on bespoke metal systems with very high X-ray contrast between the solid and liquid phases to study dendritic growth and coarsening. Recently, advanced synchrotron X-ray radiography and tomography techniques have enabled *in situ* studies of microstructure evolution during solidification of metallic alloys, although most studies have focussed on aluminium alloys. Radiographic experiments have been extensively carried out to study solidification in Al–Cu [18–20], Al–Ni [21,22], Al–Si [23,24], Sn–Bi [25,26] with thin plate-like (100–200  $\mu\text{m}$ ) samples. This enabled observations of phenomena such as columnar-to-equiaxed transition, crystal fragmentation [19,27–29], hot tearing [30] and crystallographic misorientations [22] induced by shear stress resulting from liquid flow. With the development of ultra-fast synchrotron tomography, it is now possible to reveal 3D solidification microstructure evolution over time, termed 4D imaging [31,32]. At present, this technique has been applied to Al alloys [6,7,31,33,34], providing new insights into the kinetics of the formation of several microstructural features, such as dendrites and intermetallic compounds, as well as defect formation [35,36].

At present, the application of synchrotron radiography and tomography to solidification has mainly focused on FCC alloys with a relatively inert molten phase (or one that forms a stable oxide). X-ray radiography, which requires very thin samples, imposes physical restrictions upon the growth of hcp metals like Mg due to their six-fold symmetry. The main challenge in applying *in situ* X-ray tomography to Mg is the rapid oxidation of Mg alloys under an elevated temperature, and the associated safety concerns. In the present study, the 3D morphological evolution of primary  $\alpha$ -Mg dendrites in Mg–Sn alloys is observed and quantified *in situ* using fast synchrotron X-ray tomography. For this experiment, a special encapsulation method has been developed. Results from dendrite evolution under different cooling rates (3  $^{\circ}\text{C}/\text{min}$  and 12  $^{\circ}\text{C}/\text{min}$ ) are presented in order to reveal, for the first time, 3D dendritic microstructure evolution in hcp Mg alloys.

## 2. Experimental method

### 2.1. Sample preparation and encapsulation

A binary Mg–15 wt% Sn hypoeutectic alloy was chosen for its good X-ray absorption contrast between the solid and liquid phases, allowing the solidifying 3D dendritic microstructure to be observed. The solidification range in this system is about 64  $^{\circ}\text{C}$ , from 625  $^{\circ}\text{C}$  (liquidus) to 561  $^{\circ}\text{C}$  (solidus). To fabricate the alloy, commercial purity Mg (99.99%) and Sn (99.999%) powders were mixed together in a stainless steel crucible and then melted under a protective atmosphere of  $\text{SF}_6$  and  $\text{CO}_2$ , followed by casting into a graphite mould. Cylindrical samples (dia. of 1.2 mm) were then machined from the as-cast ingot.

Mg is a strong oxidizer and in the liquid state specimens must be properly shielded. For prior *in situ* tomographic studies of Al alloys, alumina and boron nitride (BN) crucibles were used as the sample holder (e.g. Ref. [6,34]). However, for Mg alloys, the specimen needs to be sealed in an enclosed chamber that is either filled with an inert gas or under vacuum. Quartz is often used as an encapsulation material; however it reacts with Mg and is susceptible to cracking. For this study, a composite encapsulation system was developed as shown in Fig. 1a. First, the Mg sample is painted with a thin BN coating. This is then placed within a graphite crucible, followed by encapsulation within quartz. In this fashion, the Mg alloy is physically separated from the sealed quartz, ensuring safe testing.

### 2.2. Experimental setup

The X-ray tomographic experiment was carried out on the Diamond Manchester Branchline (I13) at Diamond Light Source. To conduct the experiment, a bespoke PID controlled furnace [37] was used containing X-ray windows on either side to allow the passage of X-rays, and a small hole in the bottom to allow the insertion of the sample encapsulated in quartz. Concurrently, the sample remained affixed to the rotation stage of the beamline. A schematic is given in Fig. 1b showing the specimen encapsulated in quartz inserted into a ceramic holder that is seated on the rotation stage. During the experiment, pink beam (energy range ~14–25 keV) was used to penetrate the sample, and a high speed CCD camera (PCO Edge) was used to record the images. The camera had  $2560 \times 2160$  pixels, binned  $2 \times 2$  to give  $1280 \times 1080$ , with a voxel size of 1.6  $\mu\text{m}$ . In total, 1200 X-ray projections were captured while the sample was continuously rotated from  $-90^{\circ}$  to  $90^{\circ}$ , with an exposure time of 12 ms, with each tomograph acquired in 14 s. However, at the end of each tomograph, the sample stage was rotated back to  $-90^{\circ}$ , adding an additional delay of 22 s, for a cycle time of 36 s. The 3D datasets were reconstructed using a filtered-back projection algorithm [38].

Two *in situ* experiments capturing the solidification of Mg–15 wt% Sn under different cooling rates (3, 12  $^{\circ}\text{C}/\text{min}$ ) were performed, as follows. First, each sample was gradually heated to  $-30^{\circ}\text{C}$  above the liquidus temperature and then held for 20 min ensuring complete melting. Second, each sample was cooled at the prescribed rate. During cooling, tomographic images of microstructure evolution were captured continually, at 36 s intervals, until solidification was completed.

### 2.3. Image processing

Each tomographic image was cropped and transformed to 16 bits and loaded into the Avizo<sup>®</sup> software (FEL, France) for visualizing the process of solidification in a Mg–Sn alloy. The image stacks were denoised with a 3D anisotropic diffusion filter followed by a 3D median filter, cropped to a size of  $721 \times 721 \times 1080$  pixels, i. e.  $1.15 \times 1.15 \times 1.73 \text{ mm}^3$  to remove edge effects, and then segmented to identify the solid and liquid phases using a global threshold value. Finally, a 3D region growing algorithm was applied to separate one dendrite from its neighbours for further analysis.

## 3. Results and discussion

### 3.1. Qualitative analysis

#### 3.1.1. 2D and 3D dendrite evolution

Fig. 2 shows 2D cross-sectional slices of the evolving solidification microstructures, for cooling rates of 3  $^{\circ}\text{C}/\text{min}$  and 12  $^{\circ}\text{C}/\text{min}$ , together with 3D surface renderings of individual grains. The increase in brightness (or greater X-ray attenuation) of the interdendritic liquid phase at longer times indicates the rejection of Sn from the primary phase due to solute partitioning. Note that  $T_0$ , given in images a1 and c1 corresponds to the temperature when the dendrite was first observed. Due to the 36 s interval between tomographic images, and additionally the use of a complex specimen encapsulation system, the exact specimen temperatures are not known. The listed temperature difference between the images corresponds to the difference in furnace temperature between successive tomographic images for a given cooling rate.

From the 2D slices (a1–a5 and c1–c5), it can be seen that the lower cooling rate of 3  $^{\circ}\text{C}/\text{min}$  results in a structure that is more globular in nature, as compared to the thinner dendritic structures when the cooling rate is 4 times faster (12  $^{\circ}\text{C}/\text{min}$ ). At higher

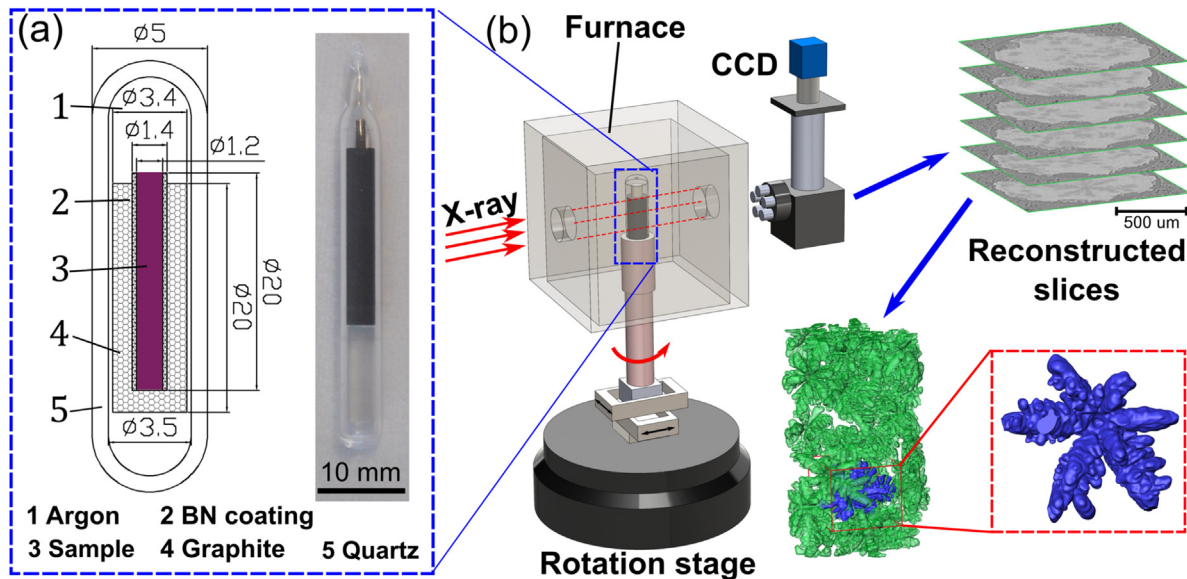


**Fig. 1.** Schematic of sample encapsulation, experimental set-up and image processing for *in situ* solidification experiment of Mg–Sn alloy: (a) sample encapsulation method - graphite then quartz, with thin BN coating on the surface; (b) experimental set-up on the Diamond-Manchester Branchline and typical results.

cooling rates attachment kinetics dominate more, whilst at slower cooling rates their influence is small, and thus dendrite evolution is dominated by solute diffusion and coarsening kinetics [2].

For both cooling rates, the initial dendritic microstructure was observed to change significantly during the free growth stage (a1–a2, c1–c2). For the 12 °C/min cooling case, there is considerable change in morphology from the first (c1) to second (c2) tomographic images (36 s interval), showing hierarchical morphology with both primary and secondary arms. The greater change is due to the higher cooling rate, hence a larger volume fraction solid change between tomograms, approximately 23%. Once the dendrite arms impinge on each other (a3,c3), lateral growth and coarsening are the dominant growth mechanisms.

The three-dimensional morphology evolution of a single dendrite is shown in (b1–b5) and (d1–d4). Hierarchical structures are present from the first observation of the dendrites, which indicates that branching based on crystallographic symmetry, and the resulting surface tension anisotropy, probably initiates early on in the growth stage of dendrites. As the temperature decreases and the solid evolves, the dendrites become thicker and the curvatures reduce. The mechanisms of secondary dendrite arm coarsening can be seen – a combination of secondary arm coalescence and curvature reduction. In the final stages, almost all the branching arms grow together, the interdendritic region is filled with solid, and the secondary arms disappear.

### 3.1.2. Dendritic morphology and branching structure

The three-dimensional dendritic morphology and branching mechanism of an isolated dendrite is shown in Fig. 3, highlighting the six-fold symmetric growth pattern with 18 branch arms. In Fig. 3a, planes were added, with the sections shown in Fig. 3a and b. The cut along the basal plane (Fig. 3b) shows the perfect six-fold symmetry expected of hcp magnesium [11,13,39]. The vertical plane cut (Fig. 3c) shows six branches that are not quite perfectly six-fold symmetric. The other two vertical plane cuts (sections 3 and 4) show a branching structure very similar to Fig. 3c.

A growth pattern can be proposed based on these three-dimensional observations of morphology and the branching structure:  $\alpha$ -Mg dendrites in Mg–Sn alloy evolves with 18 primary branch arms, six of them located on the basal plane and the

remaining 12 branches along  $\langle 11\bar{2}X \rangle$  directions off the basal plane. This growth pattern, illustrated in Fig. 3d, is in contrast with that observed in Mg–Al [13,39] and Mg–Zn [12] alloys but similar to what found in Mg–Ca alloys [40]. Specifically, in this experiment, the angles between dendrite arms growing along  $\langle 11\bar{2}X \rangle$  and along  $\langle 11\bar{2}0 \rangle$  is approximately 48°. Thus, the value of X in  $\langle 11\bar{2}X \rangle$  is approximately 2, based on the hcp structure of Mg with  $c/a = 1.624$ . This crystallography is slightly different to frequently reported  $\langle 22\bar{4}5 \rangle$  [41,42], in the literature for Mg hcp alloys (with a 6° difference in angle between these two directions). Although a few prior studies have suggested such misorientation might be caused by gravity induced mechanical forces during solidification [22,43], such forces are likely to be very small in these tiny equiaxed samples. It would seem more likely that the morphologies are more restricted by the interacting solute fields from neighbouring grains [20,44], altering the morphological shape of the dendrites, rather than their crystallographic orientation.

### 3.2. Quantitative analysis

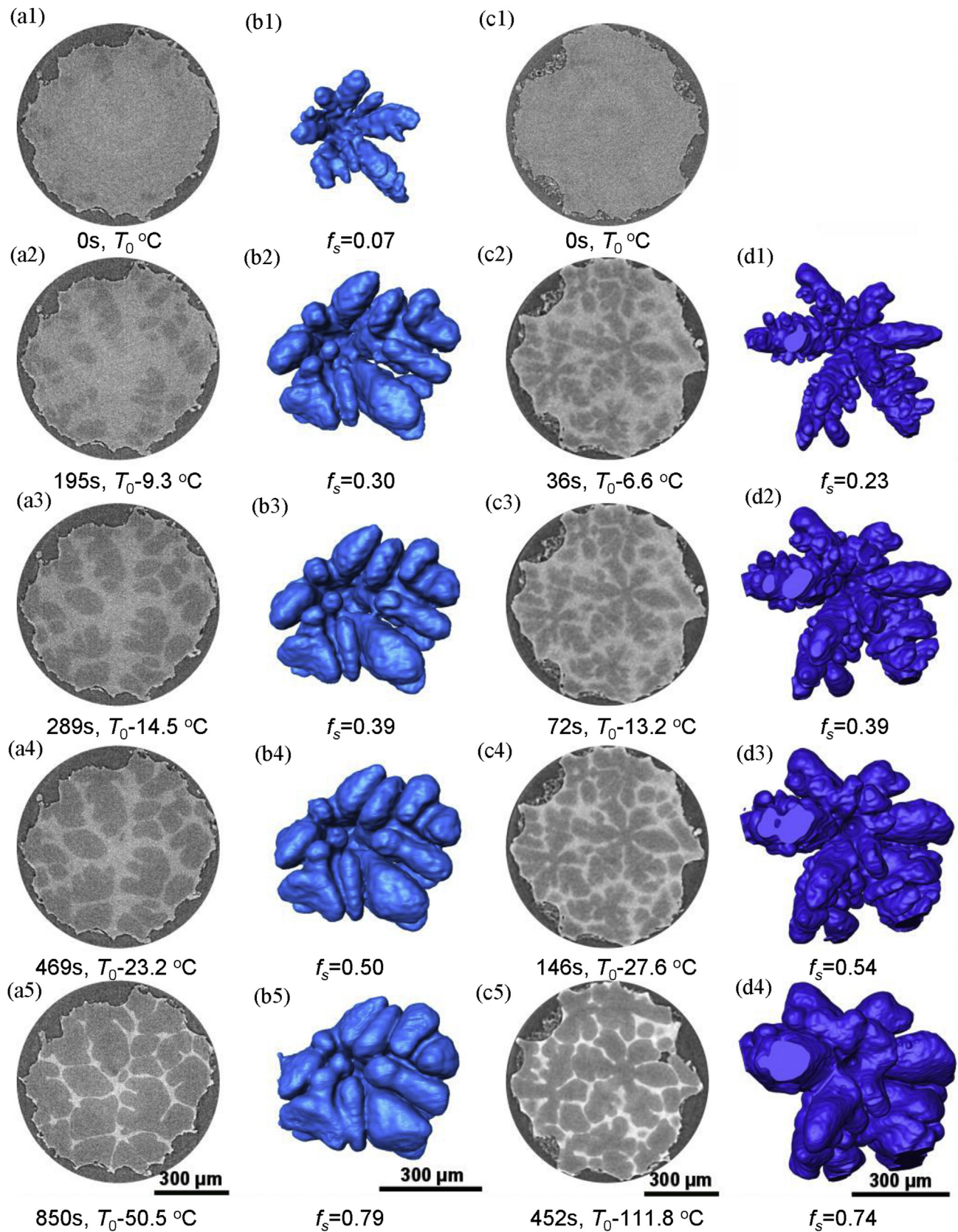
#### 3.2.1. Dendrites nucleation site selection during solidification

A significant variation in the location of dendrite grain nucleation was observed between the two cooling rates, as shown in Fig. 4. For the 3 °C/min experiment, all 34 grains nucleated near the sample surface. For the 12 °C/min experiment 27 grains nucleated, both on the surface (17) and in the middle (10) of the sample. For both cooling rates, nucleation occurs first at the surface, most probably heterogeneously on the surface oxide, but at low cooling rates the primary phase growth is not restricted, rejecting both solute and heat into the centre of the sample, reducing the nucleation potential. At the high cooling rate, growth is restricted and the thermal/solutal undercooling becomes relatively large, enabling equiaxed dendrite nucleation near the sample centre. Note more grains (34 as compared to 27) were found at 3 over 12 °C/min, whereas the reverse was expected; however, the variation is not statistically significant, and it may be that more favourable nuclei were present, or some other minor variation.

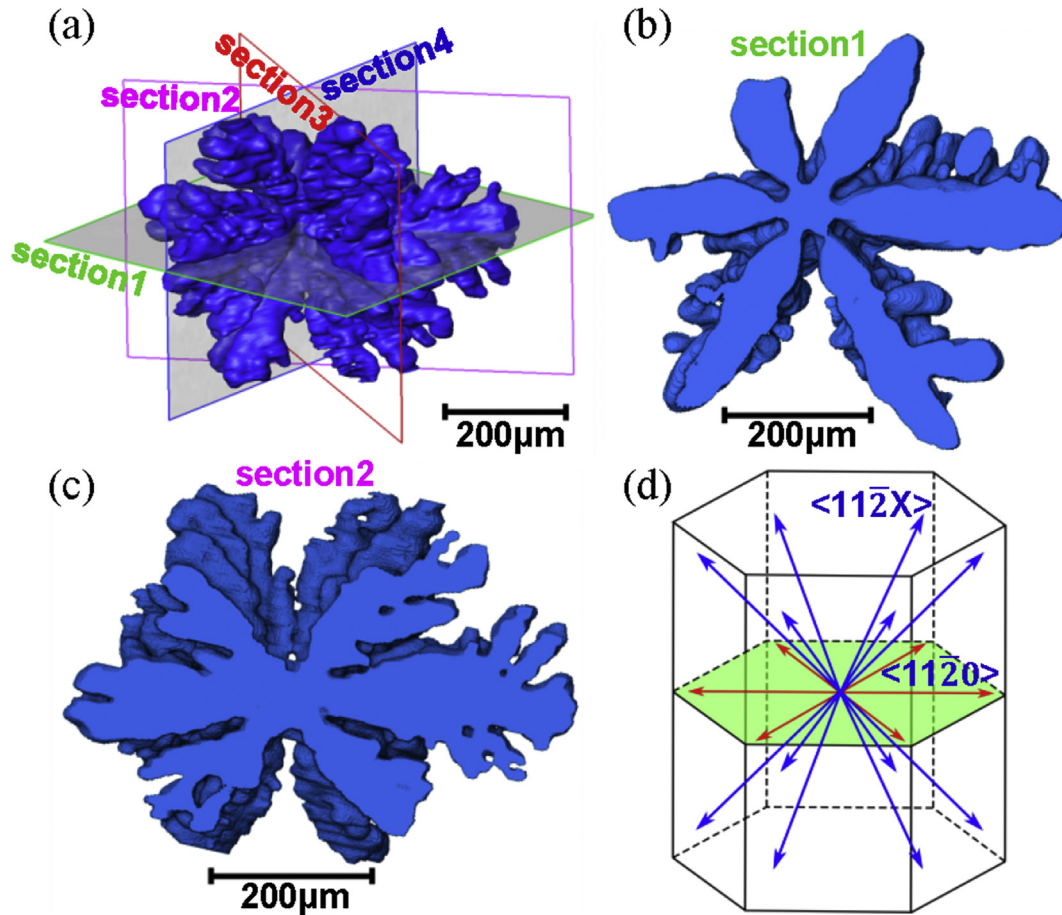
#### 3.2.2. Solid volume fraction and dendrite tip growth velocity

Fig. 5 shows a comparison of the evolution in solid volume





**Fig. 2.** 2D slices and 3D surface rendering of dendrite evolution during solidification of Mg 15wt% Sn for the cooling rates of 3 °C/min (a1–a5, b1–b5) and 12 °C/min (c1–c5, d1–d4).



**Fig. 3.** (a) Morphology and branching structure of an  $\alpha$ -Mg dendrite in Mg–Sn alloy. Eighteen branch arm growth pattern with (b) six dendrite arms shown on the basal plane (see cut-plane “section 1” in (a) and red arrows in (d)) and (c) six of the twelve arms at approximately  $48^\circ$  from the basal plane, of the twelve arms shown schematically in (d) which are hypothesised to grow along a direction of  $\langle 11\bar{2}2 \rangle$  (between  $\langle 11\bar{2}0 \rangle$  and  $\langle 0001 \rangle$ ). (For interpretation of the references to colour in this figure legend, the reader is referred to the web version of this article.)

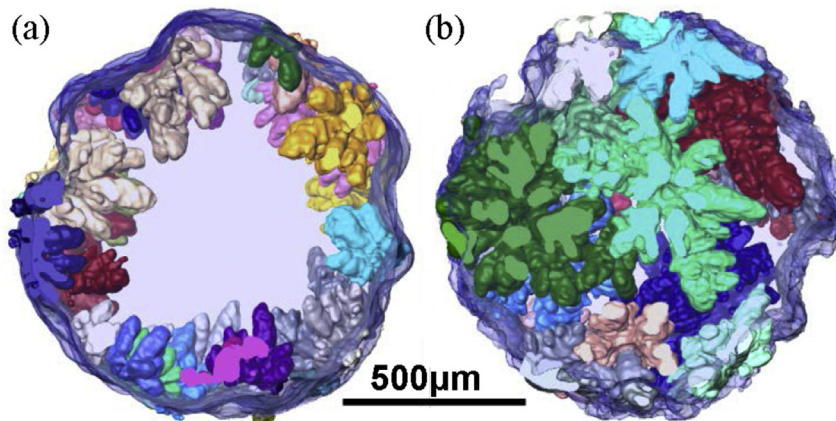


**Fig. 4.** Grain nucleation locations for cooling rates: (a)  $3^\circ\text{C/min}$ , all 34 grains nucleated near the sample surface; and (b)  $12^\circ\text{C/min}$ , grains nucleated both near the surface (17 grains) and inside the sample (10 grains).

fraction calculated from the 3D datasets for both cooling rates, combined with the Scheil equation and lever rule predictions. The partition coefficient used in the Scheil equation was taken as a constant value of 0.313. The experimental data closely follows the Scheil equation, indicating that the dendrites were growing under non-equilibrium conditions.

Although the tomography did not have sufficient spatial and temporal resolution to capture the very early stages of primary phase nucleation and growth, we can use the first frame to bound values such as primary tip growth velocity. For cooling at  $3^\circ\text{C/min}$ , the first capturing of the solid already contains approximately 7.4% solid, whilst for  $12^\circ\text{C/min}$  it is 22.6% due to the faster dendritic



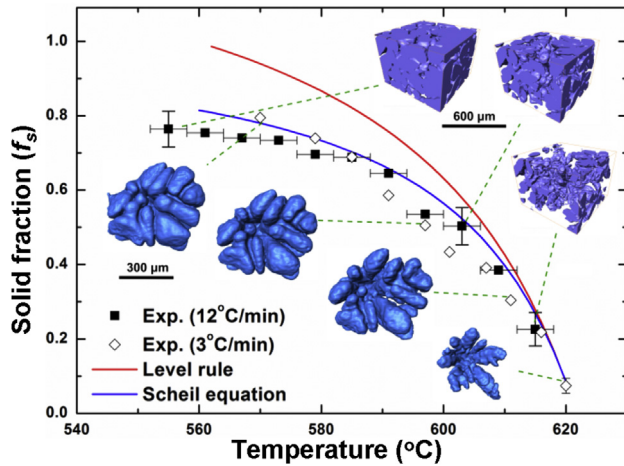


Fig. 5. Volume fraction evolution for the  $\alpha$ -Mg primary phase with temperature, compared to level rule and Scheil equation.

growth. Hence a lower limit on dendrite tip growth velocity in free growth conditions can be estimated, giving approximately 10 and 3  $\mu\text{m/s}$ , for 12 and 3  $^{\circ}\text{C/min}$  cooling rates, respectively. (Note the initial growth velocities are expected to be significantly higher than these lower bounds.) Similar results were also observed in the measurement of initial growth rates during the solidification of Al-Si [24].

The tomographic images of the 3  $^{\circ}\text{C/min}$  cooling rate sample also enabled estimation of the dendrite growth kinetics with time. Fig. 6a shows the variation in dendrite arm length ( $L-L_0$ , where  $L$  means the dendrite tip position during solidification and  $L_0$  indicates the initial position of dendrite tip) with time for the 3  $^{\circ}\text{C/min}$  sample. Fig. 6b shows the corresponding evolution in dendrite tip growth velocity with time for four dendrites from different grains within the melt. The dendrites are growing in three stages: (i) initial unconstrained growth, (ii) a constant value of the growth rate during constrained growth, and (iii) arrest once physical impingement occurs. It is evident from Fig. 6 that dendrite arm length and growth velocity vary from arm to arm. This is attributed to the influence of the adjacent dendrites in its vicinity. Based on analysis of the 3D rendering of the sample, a wider interdendritic space was observed in front of arm 2 as compared to the growth interface of arms 1, 3, and 4, which results in a longer arm length once solidification is completed.

As suggested by Bogno et al. [19], based on the 2D radiographic observation of equiaxed growth of grains in Al–Cu alloys, dendritic grain growth can be classified into two regimes: accelerating regime with a gradual increase in tip velocity and decelerating regime with gradual decrease in the dendrite tip velocity towards zero (Fig. 4a and b in Ref. [19]). In this study of Mg alloys, only the decelerating regime can be seen in Fig. 6b; the accelerating regime where the dendrite arms grow freely without any restriction from neighbouring grains is not present. This is because the accelerating growth stage happens in such a short time that it could not be observed with a 36 s interval between tomographic images [37]. The decelerating growth stage occurs due to interaction between adjacent grains, and solute rejection ahead of the growth interface resulting in dendrite growth restriction [24].

### 3.2.3. Surface curvature evolution during solidification and grain coarsening

The mean ( $H = \frac{1}{2}(k_1 + k_2)$ ) and gauss ( $K = k_1 \times k_2$ ) curvature of the surface, where  $k_1$  and  $k_2$  are the two principal curvatures at any

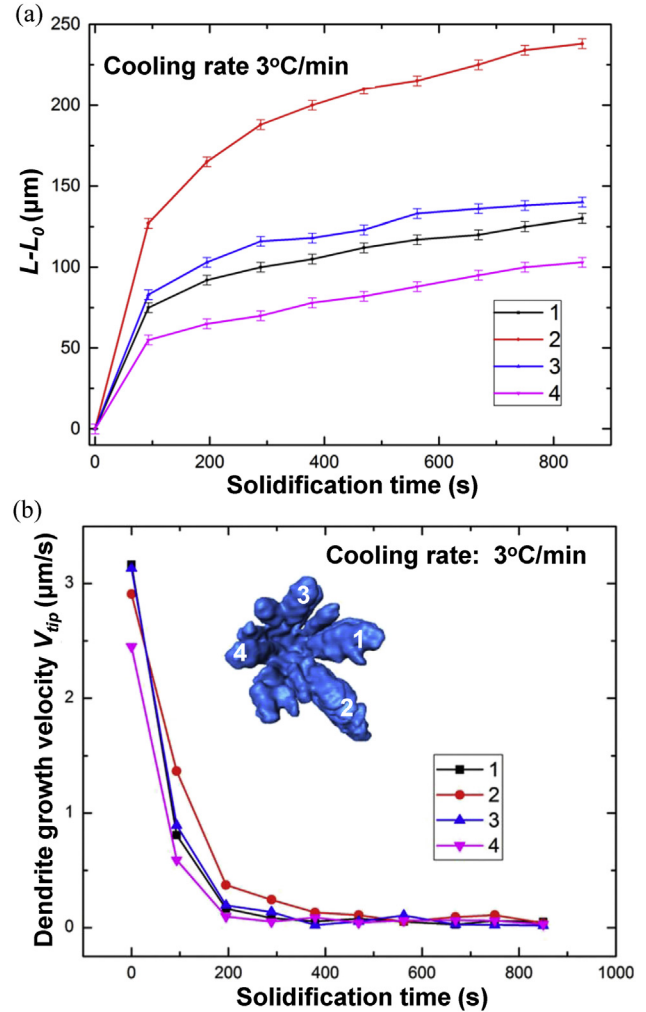
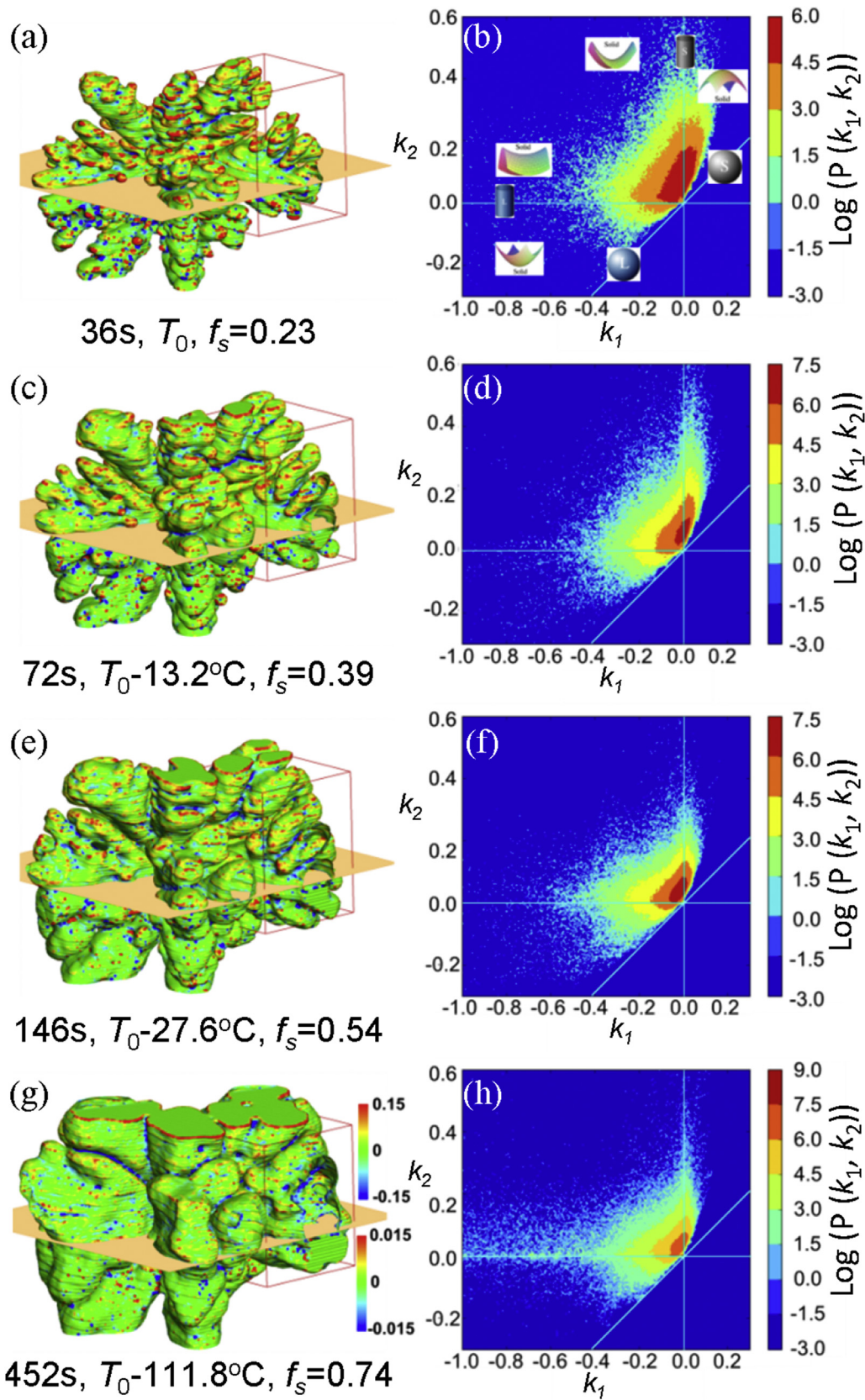


Fig. 6. (a) Relative dendrite arm length evolution during solidification and coarsening of Mg-15 wt%Sn alloys at 3  $^{\circ}\text{C/min}$ ; and (b) dendrite tip growth velocity ( $V_{tip}$ ) for 4 tips labeled in the inset image.

point in a domain, were computed (Fig. 7) to quantitatively characterize the surface evolution with increasing solid volume fraction during solidification [8,45]. As shown in Fig. 7a, c, e, g, the red areas correspond to interfaces with a large mean and gauss curvature, and are observed to coalesce with adjacent dendrite arms. The result suggests that the areas of interface with large curvature decrease with the solidification time, due to the Gibbs-Thomson effect which drives diffusion of solute from large curvature areas to small ones [46,47]. Thus, the high curvature areas disappear over time, as expected, and quantified for the first time in Mg alloys.

The evolution of the interface shape can be quantified using probability density distributions. Fig. 7b,d,f,h show the probability density of the two principle curvatures; the highest probability represents the most probable interfacial shape which exists in the dendrite. As shown in this set of figures, the majority of the interface area is located in the second quadrant with  $k_1 < 0$  and  $k_2 > 0$  which indicates a saddle-shaped or hyperbolic interface although there is a small fraction of interface with elliptical shape when  $k_1 \times k_2 > 0$ . Further, the probability of elliptical shape interface decreases with time, first transitioning to become saddle-shaped during growth and coarsening, and then to become planar-like as the peak moves towards  $k_2 = 0$  along the vertical axis.

Fig. 7a,c,e, and g, also enable discussion of coarsening mechanisms present in Mg-15 wt%Sn. Previous studies of organic



**Fig. 7.** Evolution of the mean (top half in a, c, e, g) and gauss curvatures (bottom half in a, c, e, g) of  $\alpha$ -Mg dendrite. Curvature distribution plot (b, d, f, h) of the dendrite surface during solidification ( $T_0$ , temperature when dendrite was first observed).

materials [48,49] and metallic alloys [7,50,51] during solidification, or under isothermal hold, showed that several coarsening mechanisms could coexist, that is: remelting of smaller, high curvature dendrite arms for the benefit of larger adjacent arms (*Mechanism A*) [7,52] and coalescence of neighbouring arms by the deposition of roots in between the dendrites (*Mechanism B*) [49,52]. In our study, *Mechanism A* was not identified at high cooling rate due to the fast dendrite growth; while at low cooling rate, the dendrites have grown to a large size, making the dissolution of the dendrites very slow (if any). Instead, coalescence of adjacent dendrite arms is the most frequently observed phenomena in the present study – i.e. *Mechanism B* is the dominating coarsening mechanism for these conditions.

### 3.2.4. Specific surface area evolution during solidification

The evolution of specific surface area with time of the solid phase has been widely used to quantify the overall evolution in microstructure during dendrite coarsening. Two commonly used models to quantify this microstructural evolution are Poirier's model [53,54] and Cahn and Rath's models [55,56]. Poirier's model originated from Lifshitz-Slyozov-Wagner (LSW) theory [57–59] and was then further developed assuming isothermal coarsening of rounded grains as a function of time. This model is associated with the evolving coarsening time under isothermal conditions. In contrast, Cahn and Rath's model is a function of fraction solid, rather than time. Thus it is mainly related to the temperature during solidification.

Fig. 8a plots the temporal evolution of specific surface area ( $S_v$ ) and solid volume fraction within the entire sample volume during solidification of the Mg-15 wt% Sn alloy under the two applied cooling rates. The solid-liquid interface area was extracted for both cooling rates. The values initially decrease rapidly, but then reach a steady-state. For comparison purposes, the evolution of  $S_v$  with solidification time has been fitted to the power law expression proposed by Poirier et al. [53]:

$$S_v/S_{v,0} = [1 + k \times (S_{v,0})^n \times t]^{-1/n} \quad (1)$$

where  $S_{v,0}$  is the initial value of  $S_v$  ( $1/\mu\text{m}$ ), and  $n$  and  $k$  are fitting parameters. At 3 °C/min, the evolution of  $S_v$  was fitted with  $n = 2.084$  and  $k = 2.209$ , which is roughly comparable to what was obtained in Al-Cu [60] alloys at the same cooling rate. At 12 °C/min, the fitting values for  $n$  and  $k$  were 4.219 and 4192, respectively. Although the fitted model represents the experimentally-obtained specific surface area evolution quite well, it is still difficult to relate the value of  $n$  and  $k$  to alloy composition, solidification conditions or ripening mechanism.

At the later stages of solidification, the Poirier model does not provide a good fit to the experimental data. At this point, it is better to compare against the expression suggested by Cahn [55] and Rath [56]:

$$S_v = K \times (f_s)^m \times (1 - f_s)^n \quad (2)$$

where  $K$  is a constant and  $f_s$  is the volume fraction of solid phase and  $m$  and  $n$  are fitting constants. As shown in Fig. 8b, the model fit is improved as fraction solid is increased when using  $m = 0.5$  and  $n = 0.8$ . Cahn's model is based on the spheroidal morphology during nucleation and equiaxed growth of grains in two-dimensions, while the present experiments utilized complex three-dimensional dendritic structures. Thus, at low fraction solid the model is not accurate whereas during the later solidification stage, as more dendrites arms coalesce together and the morphology becomes more spheroidal, the model fit is improved.

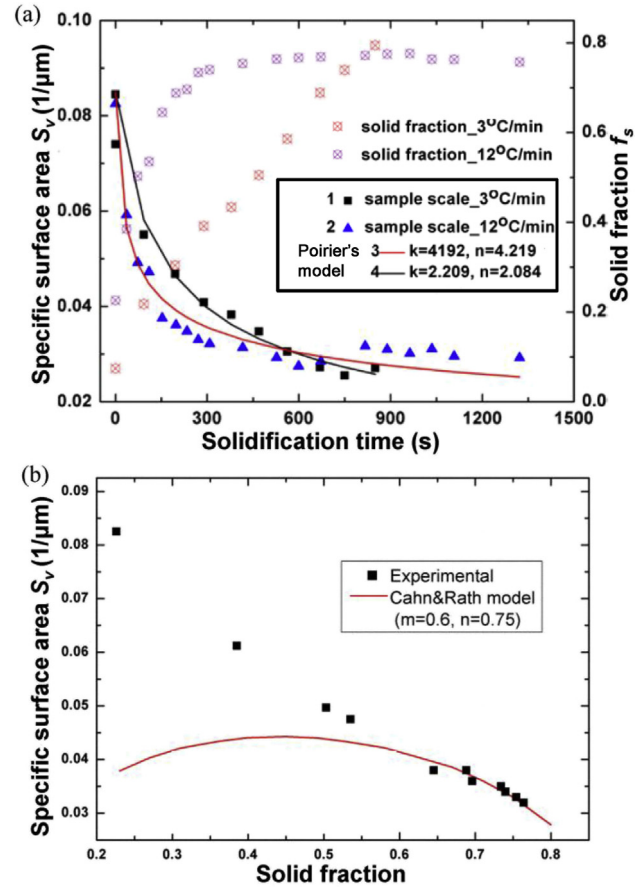


Fig. 8. (a) Volume normalised specific surface area ( $S_v$ ) and solid volume fraction ( $f_s$ ) evolution of  $\alpha$ -Mg dendrite with time during solidification, for 2 cooling rates; (b) Specific surface area as function of solid fraction, normalized by total volume, and compared to Cahn's model (cooling rate 12 °C/min).

## 4. Conclusions

Using fast *in situ* synchrotron X-ray tomography, the growth and morphological evolution of primary  $\alpha$ -Mg dendritic grains were quantified during the solidification of Mg-15 wt% Sn at two cooling rates, 3 and 12 °C/min. A novel encapsulation method was coupled with fast pink beam imaging to enable *in situ* solidification experiments in reactive Mg alloys to be performed on a synchrotron beam line.

The solidifying  $\alpha$ -Mg dendrites evolved with a six-fold symmetric growth pattern. In total, eighteen branch arms were revealed in an individual dendritic grain. Six arms grew along the basal plane ( $\langle 11\bar{2}0 \rangle$ ), and the remaining twelve in directions off the basal plane (close to  $\langle 11\bar{2}2 \rangle$ ). The cooling rate was found to play an important role in the determination of the nucleation sites, with grains only nucleating at/near the sample wall at the slower cooling rate, while nucleation was mixed surface/centre at the higher cooling rate. In both cases the nucleation was assumed to be heterogeneous.

These first 4D (3D plus time) observations of a solidifying hcp Mg alloy were quantified in terms of solid fraction, dendrite tip growth velocity, and specific surface area. The measured  $f_s$  with time/temperature was found to correlate well with the Scheil equation. Coarsening accompanied the dendritic growth. The specific surface area as a function of fraction solid compared well to the model proposed by Cahn and Rath et al. [55,56] during the late stage of coarsening, but less well in the initial growth stage,



suggesting that a more accurate model is needed to describe the evolution of the complicated dendritic structures during the solidification/coarsening process in the future.

## Acknowledgement

This work was financially supported by the EPSRC (EP/I02249X/1 and EP/M009688/1) and performed in the Research Complex at Harwell. SS and TJ gratefully acknowledge support from the National Science Foundation of China (Grants 51175292 and 51404016), the innovation platform for through process modeling and simulation of advanced materials processing technologies project (Grant 2012ZX04012-011), and the Chinese Scholarship Council. The authors also gratefully acknowledge the Diamond Light Source for use of the Diamond-Manchester Branchline under experiment MT11837-1 and technical support from Dr. Joan Vila-Comamala. Note, representative samples of the research data are shown in the figures/tables; however, the underlying raw data is not shared online due to its size.

## References

- [1] T.M. Pollock, Weight loss with magnesium alloys, *Science* 328 (2010) 986–987.
- [2] J.A. Dantzig, M. Rappaz, *Solidification*, EPFL press, 2009.
- [3] T. Haxhimali, A. Karma, F. Gonzales, M. Rappaz, Orientation selection in dendritic evolution, *Nat. Mater* 5 (2006) 660–664.
- [4] M.E. Glicksman, *Principles of Solidification: an Introduction to Modern Casting and Crystal Growth Concepts*, Springer Science & Business Media, 2010.
- [5] M.C. Flemings, Solidification processing, *Metall. Trans.* 5 (1974) 2121–2134.
- [6] D. Tolnai, P. Townsend, G. Requena, L. Salvo, J. Lendvai, H.P. Degischer, In situ synchrotron tomographic investigation of the solidification of an AlMg4.7Si8 alloy, *Acta Mater* 60 (2012) 2568–2577.
- [7] N. Limodin, L. Salvo, E. Boller, M. Suéry, M. Felberbaum, S. Gaillière, et al., In situ and real-time 3-D microtomography investigation of dendritic solidification in an Al–10wt.% Cu alloy, *Acta Mater* 57 (2009) 2300–2310.
- [8] D. Kammer, P.W. Voorhees, The morphological evolution of dendritic microstructures during coarsening, *Acta Mater* 54 (2006) 1549–1558.
- [9] J.L. Fife, P.W. Voorhees, The morphological evolution of equiaxed dendritic microstructures during coarsening, *Acta Mater* 57 (2009) 2418–2428.
- [10] E. Maire, P.J. Withers, Quantitative X-ray tomography, *Int. Mater. Rev.* 59 (2014) 1–43.
- [11] M.Y. Wang, J.J. Williams, L. Jiang, F. De Carlo, T. Jing, N. Chawla, Dendritic morphology of  $\alpha$ -Mg during the solidification of Mg-based alloys: 3D experimental characterization by X-ray synchrotron tomography and phase-field simulations, *Scr. Mater* 65 (2011) 855–858.
- [12] M.Y. Wang, Y.J. Xu, T. Jing, G.Y. Peng, Y.N. Fu, N. Chawla, Growth orientations and morphologies of  $\alpha$ -Mg dendrites in Mg–Zn alloys, *Scr. Mater* 67 (2012) 629–632.
- [13] M. Wang, Y. Xu, Q. Zheng, S. Wu, T. Jing, N. Chawla, Dendritic growth in Mg-based alloys: phase-field simulations and experimental verification by X-ray synchrotron tomography, *Metall. Mater. Trans. A* 45 (2014) 2562–2574.
- [14] Q. Li, C. Beckermann, Evolution of the sidebranch structure in free dendritic growth, *Acta Mater* 47 (1999) 2345–2356.
- [15] S.C. Huang, M.E. Glicksman, Overview 12: fundamentals of dendritic solidification—II development of sidebranch structure, *Acta Metall.* 29 (1981) 717–734.
- [16] R. Trivedi, K. Somboonsuk, Constrained dendritic growth and spacing, *Mater. Sci. Eng.* 65 (1984) 65–74.
- [17] R. Trivedi, W. Kurz, Dendritic growth, *Int. Mater. Rev.* 39 (1994) 49–74.
- [18] P.D. Lee, J.D. Hunt, Hydrogen porosity in directional solidified aluminium-copper alloys: in situ observation, *Acta Mater* 45 (1997) 4155–4169.
- [19] R.H. Mathiesen, L. Arnberg, X-ray radiography observations of columnar dendritic growth and constitutional undercooling in an Al–30wt.% Cu alloy, *Acta Mater* 53 (2005) 947–956.
- [20] A. Bogno, H. Nguyen-Thi, G. Reinhart, B. Billia, J. Baruchel, Growth and interaction of dendritic equiaxed grains: in situ characterization by synchrotron X-ray radiography, *Acta Mater* 61 (2013) 1303–1315.
- [21] G. Reinhart, N. Mangelinck-Noël, H. Nguyen-Thi, T. Schenk, J. Gastaldi, B. Billia, et al., Investigation of columnar–equiaxed transition and equiaxed growth of aluminium based alloys by X-ray radiography, *Mater. Sci. Eng. A* 413–414 (2005) 384–388.
- [22] G. Reinhart, A. Buffet, H. Nguyen-Thi, B. Billia, H. Jung, N. Mangelinck-Noël, et al., In-situ and real-time analysis of the formation of strains and microstructure defects during solidification of Al–3.5 Wt Pct Ni alloys, *Metall. Mater. Trans. A* 39 (2008) 865–874.
- [23] K. Nogita, H. Yasuda, A. Prasad, S.D. McDonald, T. Nagira, N. Nakatsuka, et al., Real time synchrotron X-ray observations of solidification in hypoeutectic Al–Si alloys, *Mater. Charact.* 85 (2013) 134–140.
- [24] A. Prasad, S.D. McDonald, H. Yasuda, K. Nogita, D.H. StJohn, A real-time synchrotron X-ray study of primary phase nucleation and formation in hypoeutectic Al–Si alloys, *J. Cryst. Growth* 430 (2015) 122–137.
- [25] B. Li, H.D. Brody, A. Kazimirov, Real-time observation of dendrite coarsening in Sn–13%Bi alloy by synchrotron microradiography, *Phys. Rev. E* 70 (2004) 2–5.
- [26] B. Li, H.D. Brody, A. Kazimirov, Real time synchrotron microradiography of dendrite coarsening in Sn–13 Wt Pct Bi alloy, *Metall. Mater. Trans. A* 38 (2007) 599–605.
- [27] D. Ruvalcaba, R.H. Mathiesen, D.G. Eskin, L. Arnberg, L. Katgerman, In-situ analysis of coarsening during directional solidification experiments in high-solute aluminum alloys, *Metall. Mater. Trans. B* 40 (2009) 312–316.
- [28] D. Ruvalcaba, R.H. Mathiesen, D.G. Eskin, L. Arnberg, L. Katgerman, In situ observations of dendritic fragmentation due to local solute-enrichment during directional solidification of an aluminum alloy, *Acta Mater* 55 (2007) 4287–4292.
- [29] R.H. Mathiesen, L. Arnberg, P. Bleuet, A. Somogyi, Crystal fragmentation and columnar-to-equiaxed transitions in Al–Cu studied by Synchrotron x-ray video microscopy, *Metall. Mater. Trans. A* 37 (2006) 2515–2524.
- [30] A.B. Phillion, R.W. Hamilton, D. Fuloria, A.C.L. Leung, P. Rockett, T. Connolly, et al., In situ X-ray observation of semi-solid deformation and failure in Al–Cu alloys, *Acta Mater* 59 (2011) 1436–1444.
- [31] O. Ludwig, M. Dimichiel, L. Salvo, M. Suéry, P. Falus, In-situ three-dimensional microstructural investigation of solidification of an Al–Cu alloy by ultrafast X-ray microtomography, *Metall. Mater. Trans. A* 36 (2005) 1515–1523.
- [32] N. Limodin, L. Salvo, M. Suéry, M. DiMichiel, In situ investigation by X-ray tomography of the overall and local microstructural changes occurring during partial remelting of an Al–15.8 wt.% Cu alloy, *Acta Mater* 55 (2007) 3177–3191.
- [33] E. Boller, A.K. Dahle, In situ study of nucleation and growth of the irregular  $\alpha$ -Al/ $\beta$ -Al<sub>5</sub>FeSi eutectic by 3-D synchrotron X-ray microtomography, *Acta Mater* 58 (2010) 5370–5380.
- [34] C. Puncrobut, A.B. Phillion, J.L. Fife, P. Rockett, A.P. Horsfield, P.D. Lee, In situ quantification of the nucleation and growth of Fe-rich intermetallics during Al alloy solidification, *Acta Mater* 79 (2014) 292–303.
- [35] S. Karagadde, P.D. Lee, B. Cai, J.L. Fife, M.A. Azeem, K.M. Kareh, et al., Transgranular liquation cracking of grains in the semi-solid state, *Nat. Commun.* 6 (2015) 8300.
- [36] K.M. Kareh, P.D. Lee, R.C. Atwood, T. Connolly, C.M. Gourlay, Revealing the micromechanisms behind semi-solid metal deformation with time-resolved X-ray tomography, *Nat. Commun.* 5 (2014) 4464.
- [37] C. Puncrobut, P.D. Lee, R.W. Hamilton, B. Cai, T. Connolly, Synchrotron tomographic characterization of damage evolution during aluminum alloy solidification, *Metall. Mater. Trans. A* 44 (2013) 5389–5395.
- [38] A.C. Kak, Image reconstruction from projections, *Digit. Image Process. Tech.* (1984) 111–171.
- [39] M. Wang, T. Jing, B. Liu, Phase-field simulations of dendrite morphologies and selected evolution of primary  $\alpha$ -Mg phases during the solidification of Mg-rich Mg–Al-based alloys, *Scr. Mater* 61 (2009) 777–780.
- [40] S. Shuai, E. Guo, Q. Zheng, M. Wang, T. Jing, Characterisation of three-dimensional dendritic morphology and orientation selection of  $\alpha$ -Mg in Mg–Ca alloy using synchrotron X-ray tomography, *Mater. Charact.* 111 (2016) 170–176.
- [41] K. Pettersen, N. Ryum, Crystallography of directionally solidified magnesium alloy AZ91, *Metall. Trans. A* 20 (1989) 847–852.
- [42] K. Pettersen, O. Lohne, N. Ryum, Dendritic solidification of magnesium alloy AZ91, *Metall. Trans. A* 21 (1990) 221–230.
- [43] B. Billia, N. Bergeon, H.N. Thi, H. Jamgotchian, J. Gastaldi, G. Grange, Cumulative mechanical moments and microstructure deformation induced by growth shape in columnar solidification, *Phys. Rev. Lett.* 93 (2004) 1–4.
- [44] D.H. StJohn, M. Qian, M.A. Easton, P. Cao, The Interdependence Theory: the relationship between grain formation and nucleant selection, *Acta Mater* 59 (2011) 4907–4921.
- [45] L. Aagesen, Phase-field Simulation of Solidification and Coarsening in Dendritic Microstructures, Thesis, Northwestern University, 2010.
- [46] R. Mendoza, Morphological and Topological Characterization of Coarsened Dendritic Microstructures, Thesis, Northwestern University, 2004.
- [47] R. Mendoza, I. Savin, K. Thornton, P.W. Voorhees, Topological complexity and the dynamics of coarsening, *Nat. Mater* 3 (2004) 385–388.
- [48] N.J. Whisler, T.Z. Kattamis, Dendritic coarsening during solidification, *J. Cryst. Growth* 15 (1972) 20–24.
- [49] P.W. Peterson, T.Z. Kattamis, A.F. Giamei, Coarsening kinetics during solidification of Ni–Al–Ta dendritic monocrystals, *Metall. Trans. A* 11 (1980) 1059–1065.
- [50] A. Mortensen, On the influence of coarsening on microsegregation, *Metall. Trans. A* 20 (1989) 247–253.
- [51] S. Terzi, L. Salvo, M. Suéry, A.K. Dahle, E. Boller, Coarsening mechanisms in a dendritic Al–10% Cu alloy, *Acta Mater* 58 (2010) 20–30.
- [52] M. Chen, T.Z. Kattamis, Dendrite coarsening during directional solidification of Al–Cu–Mn alloys, *Mater. Sci. Eng. A* 247 (1998) 239–247.
- [53] D.R. Poirier, S. Ganesan, M. Andrews, P. Ocansey, Isothermal coarsening of dendritic equiaxed grains in Al–15.6 wt.% Cu alloy, *Mater. Sci. Eng. A* 148 (1991) 289–297.
- [54] P.W. Voorhees, M.E. Glicksman, Ostwald ripening during liquid phase

- sintering-Effect of volume fraction on coarsening kinetics, *Metall. Trans. A* 15 (1984) 1081–1088.
- [55] J.W. Cahn, Significance of average mean curvature and its determination by quantitative metallography, *Trans. Metall. Soc. AIME* 239 (1967) 610.
- [56] B.B. Rath, H.I. Aaronson, D.E. Laughlin, R.F. Sekerka, C.M. Wayman, *Solid-solid Phase Transformations*, TMS-AIME, Warrendale, PA, 1982, pp. 1097–1103.
- [57] G.W. Greenwood, The growth of dispersed precipitates in solutions, *Acta Metall.* 4 (1956) 243–248.
- [58] I.M. Lifshitz, V.V. Slyozov, The kinetics of precipitation from supersaturated solid solutions, *J. Phys. Chem. Solids* 19 (1961) 35–50.
- [59] C. Wagner, Theorie der alterung von niederschlagen durch umlosen (Ostwald-reifung), *Z. Fur Elektrochem. Berichte Der Bunsenges. Fur Phys. Chem.* 65 (1961) 581–591.
- [60] S. Terzi, E. Boller, L. Salvo, M. Suéry, In situ X-ray microtomography study of the solidification and remelted microstructures of Al-Cu alloys, *Int. J. Cast. Met. Res.* 22 (2009) 275–278.